3 Laser and Target Setup

In this chapter the main components of the experimental setup, i.e. the laser system and the liquid-jet apparatus, will be presented. Therefore it is divided into a first part which is dedicated to generation, amplification and modification of ultrashort laser pulses at high repetition rates and a second part that discusses the most relevant technical and scientific aspects of liquid–jet targets.

3.1 Generation of High-Repetition Rate fs-Laser Pulses in the Milijoule Range

A number of major innovations within the last two decades have led to enormous progress in the field of generation and amplification of sub-ps laser pulses. A few milestones shall be mentioned here; further information can be found in a number of review articles (see, e.g. Chériaux and Chambaret [CC01]):

- Chirped pulse amplification (CPA): The principle of CPA poses a major breakthrough in amplification technology as it allows to reduce the enormous peak power of the fs-pulses, which would otherwise limit the output energy because of intensity dependent pulse distortions and damage of the amplifiers components [SM85].
- The development of new crystalline laser materials, such as titanium-doped sapphire (Ti:Sa), opened up the era of small, reliable and efficient fs-lasers [PM92].
- The discovery of the self-mode locking in Ti:Sa-crystals by W. Sibbett et al. [SKS91] changed the 'art of alignment' of sub-ps laser oscillators into a negligible problem.

Now, after two decades of rapid development in ultra-short laser science, oscillators with pulses as short as 12 fs (e.g. Femtosource scientific, Femtolasers, Vienna) and amplifiers featuring miliJoule pulse energies at 1 kHz repetition rate (e.g. Hurricane, Spectra-Physics, Inc.) are available commercially. This allows fs-laser applications to increase rapidly in number and quality (e.g. in the medical field [SS01], [JLK99]). On the other hand, laser physicists can focus on new technologies such as the generation of even shorter pulses [PTB01], [DHK01], or the generation of (sub-)ps radiation at much shorter wavelengths for

applications like XUV-lithography [TFG99], [VOG01] or material analysis [CRP99], [CWS99]. The experiments presented here belong into the latter category, in that the generation of ultrashort pulses of hard X-rays at Kilohertz repetition rates was investigated. This project included the setup and development of a laser system consisting of a Ti:Sa-oscillator and multi-stage Ti:Sa-amplifier. This section describes the components of the system in detail. Key performance parameters of this system will be discussed.

3.1.1 The Oscillator

The setup of the fs-laser oscillator (Fig. 3-1) corresponds essentially to the setup[1] of Pshenichnikov et al. [PBW94], [WB97]. The laser cavity is defined by the mirrors M1 (high reflection coated) and M4 (output-coupler with a reflectivity of R=95%). M2 and M3 are curved (r=100 mm) mirrors which focus the laser beam into the Ti:Sa crystal. The crystal is relatively short (4 mm) to reduce dispersion and highly doped (0.15%) to maintain amplification. The oscillator is pumped by a Millenia Vs (Spectra Physics) continuous-wave all-solid-state laser. Its output wavelength and pump power are 532 nm and 5 W, respectively. This green pump beam is focused by a plano-convex lens (f = 100 mm) into the laser crystal where it generates radiation at about 800 nm. The angles (15.2°) of the beam at M2 and M3 are chosen to compensate the astigmatism introduced by the laser crystal [WB97], [KID73]. Although the processes that lead to fs-pulse generation in such a cavity are well-known and described in review articles [SCB94] as well as in textbooks [DR96], [WK99], [SH98], the

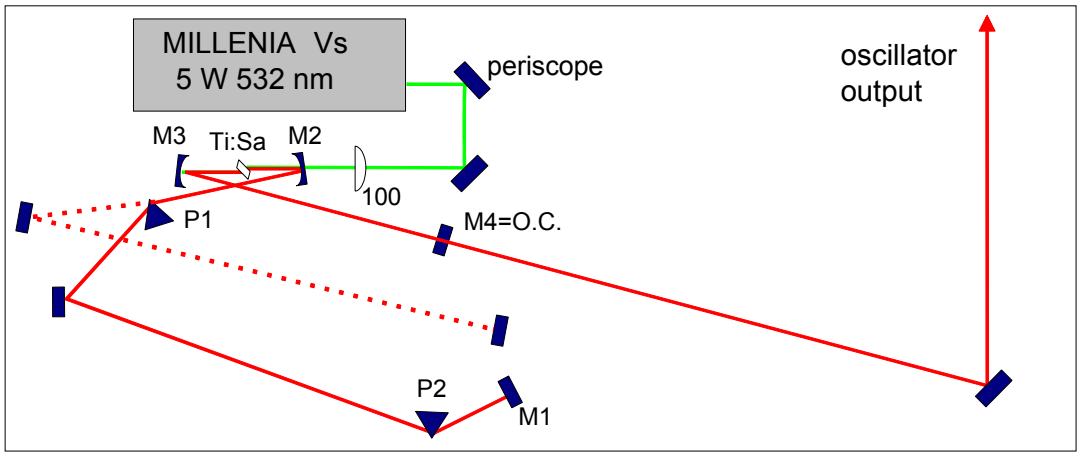

Fig. 3-1 : Schematic diagram of the Ti:Sa-laser oscillator. M1 – high reflecting end mirror; M2, M3 - curved mirrors, M4 - partially reflecting output-coupler, P1, P2 – prisms. The frame outlines the limits of a 60 cm × 120 cm breadboard.

[1] Initially, a cavity dumper as demonstrated by Pshenichnikov et al. was also set up. In comparison to the almost maintenance-free oscillator it was found to be more alignment sensitive. Hence, for the sake of stability it was subsequently not used.

main effects should be repeated here to improve the understanding of the system.

The focused laser-modes undergo self-focusing in the laser crystal by forming a Kerr-lens. Since the Kerr-lens is intensity dependent, its refractive power is larger for shorter (stronger) pulses and hence, stronger peaks in the noise have a smaller beam waist. The pump beam has to be focused tightly into the laser crystal (focus diameter smaller than that of the cw-laser mode beam waist), so that a reduction of the size of the oscillator mode by the Kerr-lens leads to a better match with the pump beam. Consequently, low-energy laser modes gain less amplification than stronger ones and ultimately a solitary peak grows out of the cw noise (passive self-mode-locking)[1].

In addition to self-focusing (Kerr-lens), the pulsed radiation undergoes a second, nonlinear effect in the Ti:Sa-crystal: self-phase-modulation. Depending on the peak-intensity, this effect may broaden the spectrum of the laser pulse (limited by the amplification bandwidth of the crystal) to a FWHM of up to 50…100 nm. This spectral width is required for the creation of ultra-short laser pulses. Because of the different velocities of the spectral components in the crystal material (group velocity dispersion GVD), the pulse is temporally broadened each time it traverses the laser crystal. By insertion of prism P1 (Fig. 3-1) into the beam path, a line with the inverse dispersion characteristics is introduced. Alternatively, P1 can be removed and the oscillator is operated in cw-mode without GVD compensation. A proper distance between P1 and P2 balances the GVD induced by the crystal and the traversed prisms[2]. Under these conditions a solitary short pulse circulates in the cavity. Every time it reaches M4, a small part (3…10%) is coupled out by the limited reflectivity of M4. Their temporal distance T is defined by the cavity length L: $T = 2L / c$. For a cavity length of 1.74 m this results in 12 ns pulse-to-pulse delay or 86 MHz repetition rate. Using an output mirror of $R = 0.95$ more than 0.5 W (i.e. 6 nJ per pulse) of average output power is generated. Fig. 3-2. shows the transient of an output pulse and its spectrum. Assuming a gaussian shape and a central wavelength at 783 nm (FWHM is 60 nm), the time-bandwidth product of this pulse is found to be 0.470. This is close to the theoretical limit of 0.441 for gaussian pulses. It proves that the remnant higher-order chirp of the pulse is small.

[1] This mechanism needs a distortion for starting. More reliable is the use of semiconductor-saturable-absorber (SESAM) mirrors [JKM97].

[2] The prisms must be non-symmetrically cut (fused silica, roof angle 69.06°) to enable an incident angle close to the Brewster angle for minimal cavity losses.

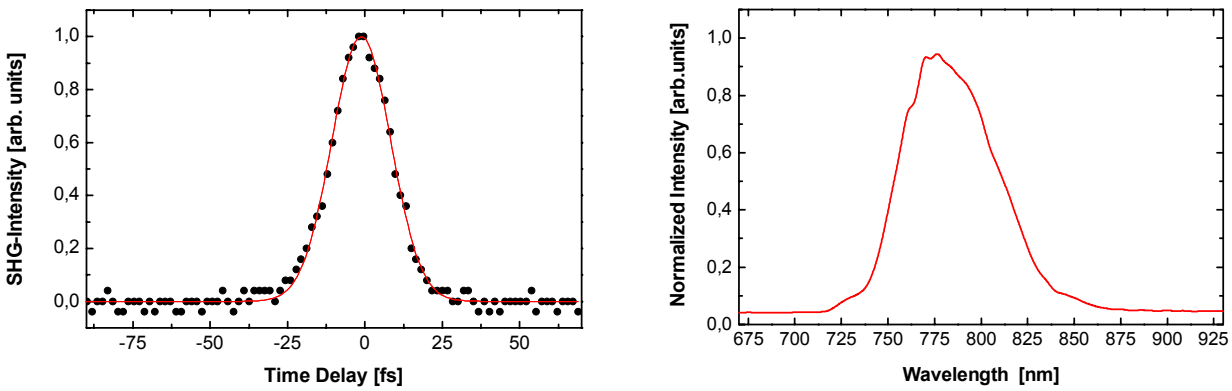

Fig. 3-2 : Autocorrelation trace with a gaussian fit-curve (left) and spectrum (right) of the Ti:Sa- laser oscillator pulses. The pulse length after deconvolution is 16 fs (FWHM) and the spectral width is 60 nm.

3.1.2 High-Repetition Rate Amplification of fs-Laser Pulses

The basic theory for amplification of ultrashort pulses can be found in textbooks (see e.g. [DR96], [WK99]). In the late 1980s solid state materials, such as Ti:Sa, Nd:glass, alexandrite, and Cr:LiSAF [PM92], [PM94], were introduced in the amplification of ultrashort laser pulses. A few years later, the first amplifier with kHz repetition rate were realized using Ti:Sa-crystals [SSM91], [SKM93]. Ti:Sapphire features several characteristics which make it the 'workhorse' of ultrashort pulse generation and amplification. These include a high damage threshold (~8-10 J/cm²), a high saturation fluence (~1Jcm²) and a high thermal conductivity (~46W/mK at 300 K) [CC01], [PM92]. More importantly, it offers a broad gain-bandwidth of about 200 nm centered at 790 nm, which supports generation of ultrashort laser pulses. Its broad absorption near 500 nm enables pumping with frequency-doubled YAG-lasers.

The basic layout of the two most popular amplifier schemes is given in Fig. 3-3. The first type, the regenerative amplifier, is very similar to a laser cavity. In the setup with two Pockels cells the first (PC1) switches 'on' for a few ns, enabling one *seed* pulse (taken from the ~90 MHz pulse train of the oscillator) to enter the Ti:Sa-crystal after it traversed the Pockels Cell twice (quarter-wave voltage). Consecutive pulses from the oscillator are reflected, while the seed pulse can cycle the cavity and undergo amplification due to its rotated polarization. After about 20 round-trips gain saturates and the second Pockels cell is turned 'on'. Then the pulse is coupled out by reflection on the polarizer (again, double–pass in PC2 with quarter-wave voltage). The first Pockels cell is started again after a time defined by the repetition rate of the

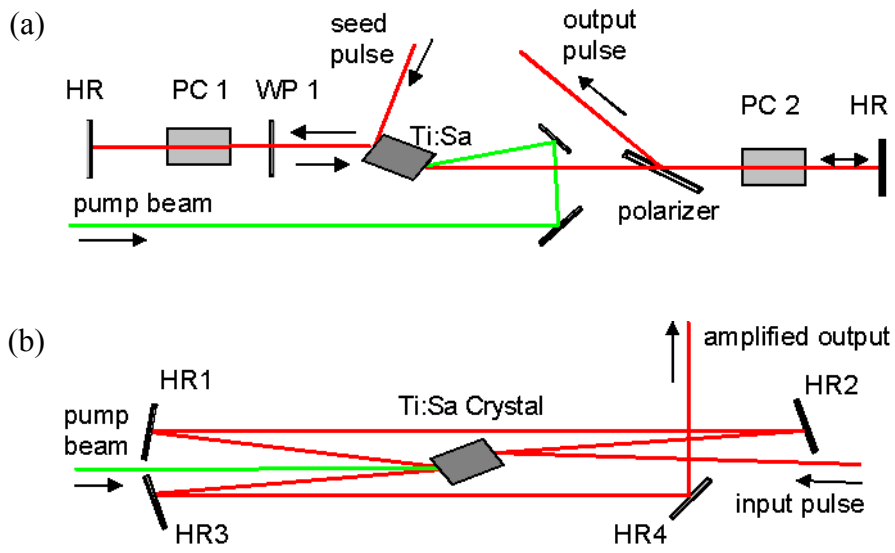

Fig. 3-3 : (a) Regenerative amplifier layout. (b) Multipass amplifier layout. (HR: high-reflection mirror, PC: Pockels cell).

(green) pump laser. At 1 kHz pump rate, the amplification takes about 200-300 ns and the system waits for the remainder of 1 ms for the next cycle.

The (roughly) 20 round-trips are usually enough for amplification from the nJ- level of the seed pulses to the mJ level of the output, i.e. a gain of about 10^6. This is one reason why regenerative amplifiers are a favored solution for pre-amplification schemes (as will be shown later in the Spitfire-system used for our experiments).

The second type of amplifier differs from the regenerative in what its name suggests: the pulse passes through the amplifying medium several times without the use of a cavity. Each round-trip the beam path in the crystal is changed slightly, so the overlap between pump-beam and seed beam is not as good as than in the regenerative type. Advantages of a multi-pass amplifier are a lower amplified spontaneous emission (ASE) and less accumulation of higher order phase distortion, so shorter pulses are easier to obtain upon recompression. A serious disadvantage of regenerative amplifiers is the appearance of pre-pulses. When the pulses cycle in the cavity of the regenerative amplifier, a small but finite part is always reflected on the polarizer. This may be increased by small misalignment of the Pockels cells or the polarizer or just by thermal distortions in these components. Because of the nature of the amplification process, these pulses precede the main output pulse and grow simultaneously to the pulse cycling in the cavity. Koechner [WK99] gives a rather conservative number of 1:20 for a typical contrast between main and pre-pulse. The Spitfire system used here is specified for a contrast of 1:100 [SPL02] and continuous observation of pre-pulses using a

fast silicon-diode (Thorlabs, DET210) showed only one pre-pulse with a contrast of about 1/500 (worst cases 1/200). The distance of 10 ns from the pre-pulse to the main pulse confirms its origin (10 ns is the characteristic cycle period defined by the cavity length of the regenerative amplifier).

Before proceeding to the next section, a -more technical- limitation should be mentioned: the pump laser. Amplifier schemes of the discussed types usually rely on commercial pump lasers with only small modifications (large-scale facilities excluded). For Ti:Sa-crystals these are Ar-ion- or frequency doubled neodymium lasers. Although diode pumping introduced a lot of advantages in the latter systems recently, diode-pumped systems are still limited to energies of about 20 mJ per pulse (at 1kHz). Hence, even efficient generation of 20 mJ pulses (20 fs) at 1 kHz requires a battery of 5 pump lasers [BS00]. The rapid progress in the development of green diode-pumped lasers may widen this bottleneck in the near future; the recent announcement of a device with 75 W green power at 10 kHz repetition rate (Corona, Coherent Inc.) is already one step in this direction.

The multi-stage 1 kHz amplifier system for the experiments presented in this work is sketched in Fig. 3-4. It fits on a 3 m × 1.5 m vibration-isolated optical table and comprises - beside the oscillator - two different sub-systems:

- Spitfire (Spectra Physics, Inc.): A commercial 1 kHz-amplifier system for ultrashort pulses including a pulse stretcher, a regenerative amplifier, a 2-pass power amplifier and a compressor. It is pumped by a 20 W-Merlin pump laser (Spectra Physics, Inc.)

- 2-pass post-amplifier (built at MBI by Dr. N. Zhavoronkov) with a separate pulse compressor and one 20 W pump laser (GM30, Photonics Industries, Inc.).

The stretcher in the Spitfire system uses a grating-telescope-scheme as suggested by Martinez [OM87] with one grating (1200 mm^{-1}) and all-reflective-optics. The regenerative amplification stage and the consecutive 2-pass power amplifier work as described above and as indicated in Fig. 3-3. Pulse compression in the Spitfire (as well as in the post-amplifier) utilizes a grating (1500 mm^{-1}) and two roof mirrors as suggested by Treacy [ET69]. Before the compressor stage of the Spitfire system, a beam-splitter is introduced which guides about 35% (or 1 mJ) of the pulse power after the power-amplifier to the post-amplification stage. The two-pass post-amplifier is set up as indicated in Fig. 3-3b; a thermo-electric cooler keeps

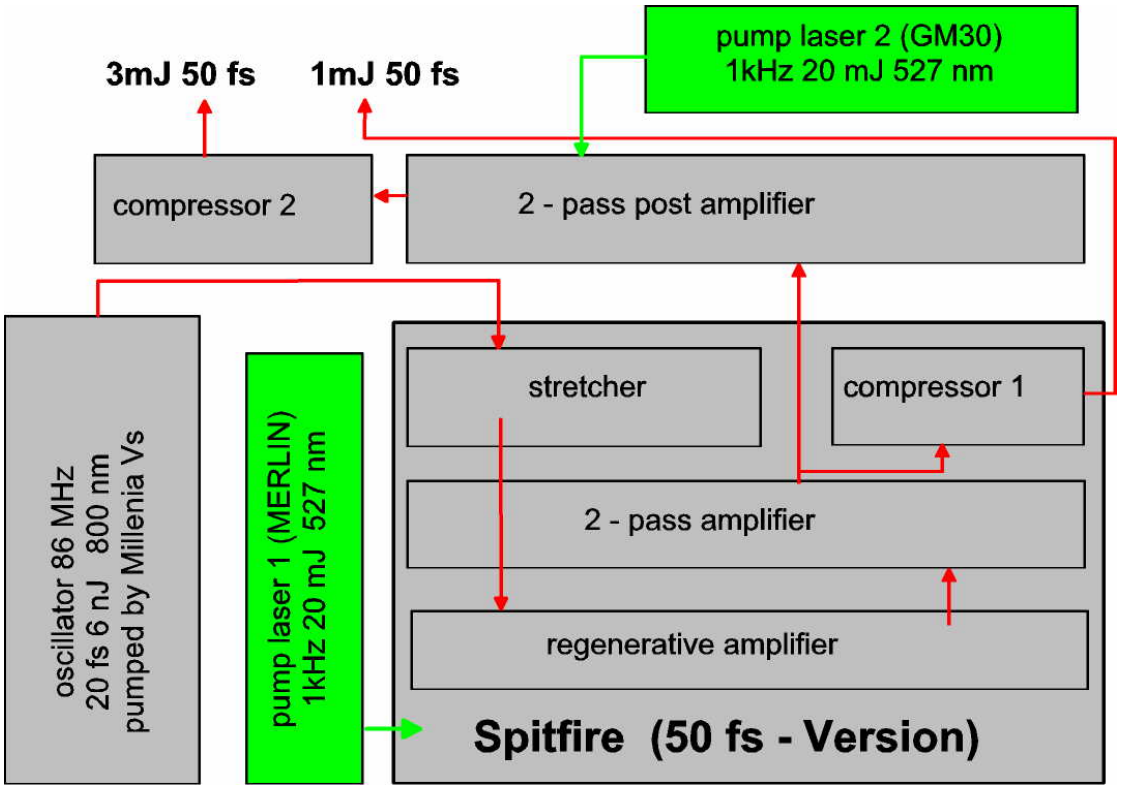

Fig. 3-4 : Laser and amplifier setup for the generation of two separate beams of 50fs-laser pulses at 1 kHz repetition rate with energies of 1 mJ and 3 mJ, respectively.

the crystal at –30°C). It increases the energy of the extracted pulse from 1 mJ to about 5 mJ[1]. After compression in the separate compressor 2, the energy is reduced to 3 mJ. The output energy after compression (compressor 1) of the Spitfire-system is 2 mJ without beam seeding of the post amplifier and 1 mJ otherwise.

This scheme allows the generation of two separate pulses with 50 fs length and 1 kHz repetition rate for pump-and-probe experiments. For this application the separate compressor stages offer a particular advantage: independent pre-compensation of dispersion in the two beam-lines.

The final output pulse from the post-amplifier was characterized temporally, spectrally and spatially. Fig. 3-5 shows a transient of the amplified pulse as determined by SHG-autocorrelation along with the corresponding spectrum. The spectral width after all three amplification stages is 27 nm (FWHM) and the almost Gauss-shaped spectrum is centered at 298 nm. The temporal width was determined to 57 fs and 50 fs (FWHM, deconvoluted from the auto correlation function (ACF)assuming a gaussian profile) for a 3 mJ-pulse after the post amplifier and for a 2mJ pulse after the Spitfire system, respectively. The pedestal in the

[1] After the experiments shown here an upgrade of the post-amplifier with cooling down to –70°C and a second pump-laser was starting. This should increase the output before compression to 10…20 mJ.

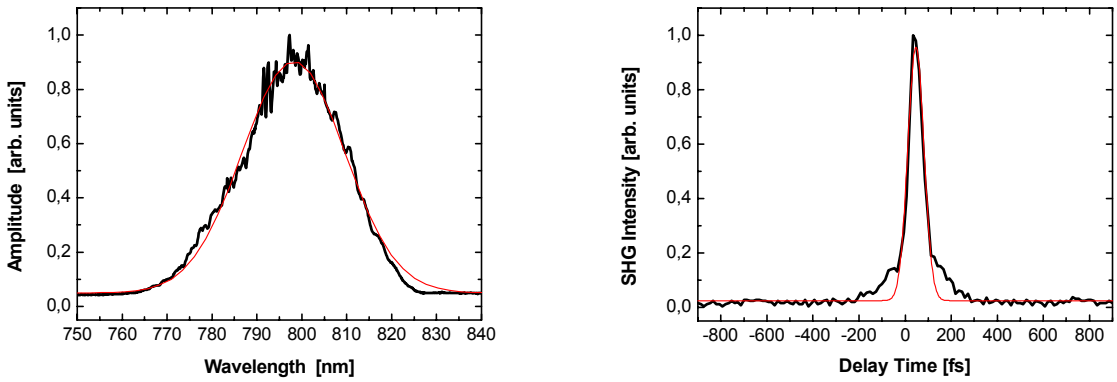

Fig. 3-5 : Spectrum and auto-correlation of the amplified laser pulse (*E* = 3 mJ). A gaussian fit is superimposed on both traces.

temporal shape is due to higher order phase distortion and could not be removed with either of the grating-based pulse-compressors.

The spatial distribution of the laser pulse in the focal plane of the lens L1 (f_1 = 75 mm, plano convex, 25.4 mm diameter) was measured with a SPIRICON LBA 100A (Spiricon, Inc.) beam analysis system including a Pulnix TM7CN CCD-camera. For this purpose the amplified laser pulses were attenuated by two consecutive reflections on fused silica prisms and by a stack of optical neutral-filters. The focal plane of the test-lens L1 was projected onto the CCD camera with an aspheric lens L2 (f_2 = 11 mm). The distance between the analyzing lens L2 and the CCD plane was determined to be d=274 mm. Defined by the size of one CCD-pixel (8.4×9.8 µm²) the resolution of the system can be estimated to 0.34µm and 0.39 µm in X- and in Y-direction, respectively. The LBA-100A beam diagnosis system can compute the center and the orientation of an elliptical beam along with the diameter of the major and minor axes. Furthermore, it can perform a least square fit to a Gaussian profile (using two univariate normal equations for the pixels along both axis [SPI92]). Table 3-1 shows the elliptic axes calculated using the gaussian fit procedure and assuming 86% energy confinement. These values are divided by the magnification factor $M=f_2/(d-f_2)$ of the optical system and presented in the third column as focal parameters (i.e. minor and major axis of the elliptic laser beam in the focal plane of the test lens L_1).

The uncoated lens induced a loss at full laser power (at 800 nm) of 15%. This allows calculation of the focal intensity on the target (see, e.g., Fig. 4-5) to 3.1×10^{16} W/cm² (E = 2 mJ, 50 fs) and 4.6×10^{16} W/cm² (E = 3 mJ, 60 fs), respectively. A graphical presentation of the focal spot is given in Fig. 3-6: this required conversion of the raw CCD-image (Fig. 3-6 b) to

relative intensity numbers (Fig. 3-6 c) using MicroCal Origin. A Gaussian distribution was fitted to horizontal and vertical sections of the relative laser-intensity (Fig. 3-6 a) and d).

Table 3-1 : Results of beam profile measurements using a test-lens with f =75 mm.

Energy per laser pulse	Elliptic axes on CCD (86% Energy confinement) Long axis	Short axis	Calculated focal parameter (ellipse) (86% E)		Focal area (elliptical)	Intensity (86% E)
E [mJ]	**2A** [µm]	**2B** [µm]	**2a** [µm]	**2b** [µm]	**A** [cm²]	**I** [W/cm²]
1.5	280	248	11,7	10,4	9,5E-07	2,2E+16
2.5	252	222	10,5	9,3	8,7E-07	4,5E+16

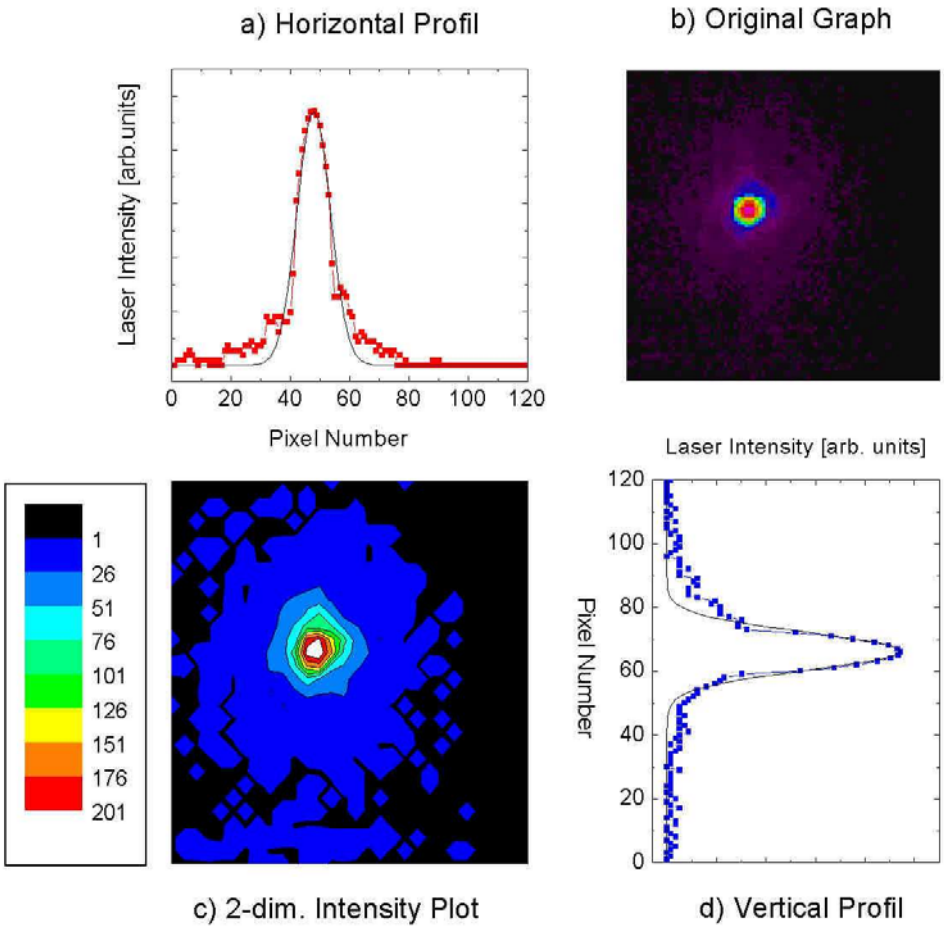

Fig. 3-6 : Beam profile of the amplified laser pulse. Shown are a) a horizontal and d) a vertical intensity trace through the center of the intensity distribution c). Figure b) is the unprocessed image as derived with the CCD-camera. The size of one CCD-pixel is 8.4µm × 9.8 µm (corresponds to 0.34µm × 0.39 µm after de-magnification).

3.1.3 Adaptive Modification of Ultrashort Laser Pulses

Since temporal structure and spatial quality of the laser pulses are crucial for the efficient generation of a plasma, a few methods for adaptive correction of these parameters will be discussed in the following. The term *adaptive* refers in this context to the usage of a closed-loop optimization scheme (Fig. 3-7), which typically comprises:

- A detector sensitive to the parameter that is to be optimized (optimization parameter OP)
- A computer system for evaluation of the OP and the control of the modulator
- A laser-pulse modulator.

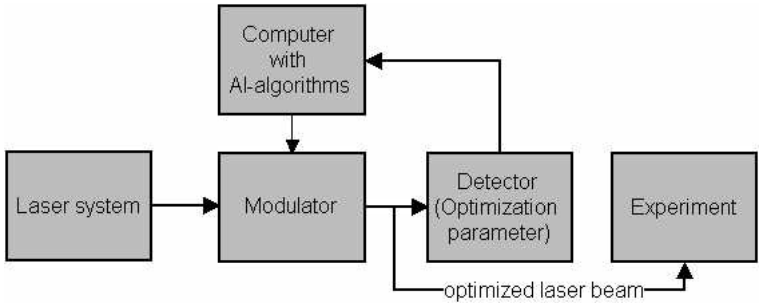

Fig. 3-7 : Closed-loop optimization scheme for laser-beam parameters.

Closure of the feed-back loop is not required; if it is closed, however, algorithms developed in the field of artificial intelligence (AI) for general optimization problems can be employed (e.g. genetic algorithms [DG89], [SSK96]). If the optimization parameter is taken directly from the experiment, one enters the broad field of coherent control (of, e.g., molecules [JR92] or chemical reactions [ABB98]).

For the sake of simplification, the different optimization methods may be classified by the optimization parameter OP. Relevant OPs are: spatial beam profile, pulse spectrum and temporal pulse shape (i.e.the spatial, spectral and temporal phases and amplitudes of the electromagnetic field distribution of the laser pulse).

The spatial profile of the laser beam is subject to wave-front aberrations in multi-stage high-power Ti:Sa amplifiers. A number of different effects contribute to this problem: imperfections in optical elements, thermal distortions in the amplifier crystals, non-linear effects (e.g. the intensity-dependent index of refraction n_2), etc. Although cooling can reduce at least the thermal distortion, another approach has become popular in recent years. Deformable mirrors (DM), known from astronomy for the correction of atmospheric distortions, were introduced for an adaptive and spatially resolved correction of the wave

front of amplified laser pulses [DCF98], [PPS99]. Wave front metrology (for the optimization parameter) is a non-trivial problem, but it can be solved with a Hartmann-wave front detector [EH01].

The correction of the spectral and temporal[1] pulse profile may be discussed simultaneously, since spectrum and temporal shape are just Fourier-transformed representations of the same physical phenomenom, namely the electro-magnetic field. Consequently, they can be corrected with the same setup. Typical problems to be solved by such a modification of the laser field are:

- Compensation of higher order phase dispersion (phase modulation),
- Compensation of gain narrowing by appropriate modulation of spectral amplitudes.

These tasks require a phase modulator which is placed in a Fourier plane of the beam, i.e. a plane where the different frequencies of the laser pulse are transversely spread out. Fig. 3-8 shows a typical arrangements incorporating a deformable mirror [CC01], [ZMB99] and a liquid crystal modulator (LCM) [AW00]. Alternatively, similar effects can be achieved using an acousto-optical modulator [DTW97], [VLC00]. In all these schemes, the spectral phase of $E(\omega)$ can be manipulated. The precision is given by the lens-grating parameters and the spatial variability of particular modulator, respectively. Special setups utilizing e.g. two mirrors (at least one out of the Fourier plane [BPW02]) or two liquid-crystal arrays and a polarizer [AW00] allow for separate control of the phase and amplitude of the laser field $E(\omega)$.

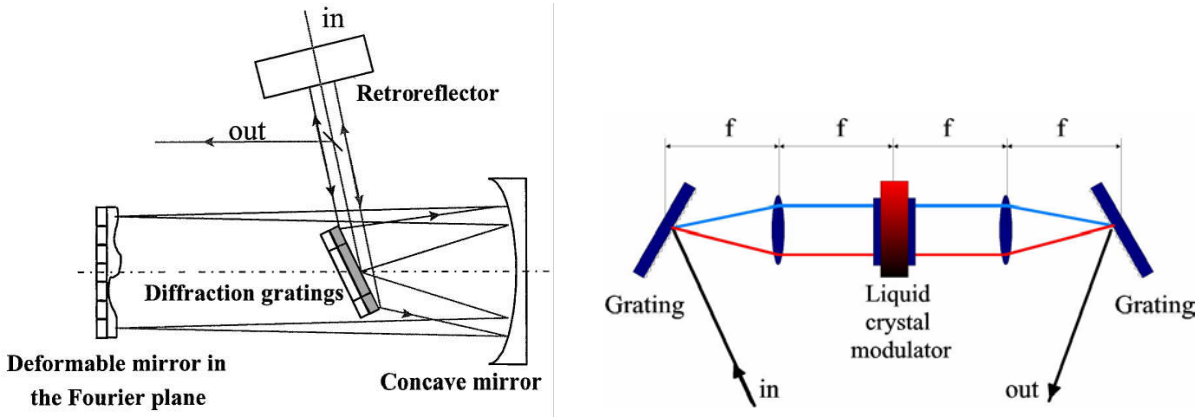

Fig. 3-8 : Pulse shaping using a) deformable mirror [CC01], and b) a liquid-crystal modulator.

A LCM system of the latter kind had been tested on the laser system in our laboratory. Beside positive effects like the correction of higher order dispersion, it (unfortunately) introduced a number of new problems. Placed between oscillator and amplifier, it exhibited a strong

[1] The problem of pre-pulses is excluded here. Optimization of pre-pulse parameters was done, e.g., by Feurer [TF99].

sensitivity to minimal changes of the oscillator spectrum such as a shift of the peak frequency by a few nm, which occurs whenever the oscillator is re-started. While this impacts the amplification only minutely, such a change requires an entirely new LCM-phase setting. Another problem occurred due to the discrete spatial structure of the LCM: phase differences between adjacent pixels lead to diffractive effects and hence, to spectral inhomogenities in the laser beam before and after Fourier-(back-) transformation. This effect might also be responsible for a reduced temporal contrast, which was seen on a ps-scale.
While the LCM turned out to be a useful instrument for experiments requiring fine-tuned pulse trains [SBT02], it offered no substantial improvement for plasma generation and, hence, was excluded in from experiments described below.

3.2 The Liquid Jet Target

In the early days of high-field laser research, single-shot experiments dominated and the target could be replaced after each shot. In the 1990's the 10-Hz laser systems entered the laboratories and targets had to be movable to present a fresh surface to each shot. Because of the tight focusing of the lasers, the target position had to be maintained on a scale of only a few microns. This problem was solved for a number of different target systems: wires [GUO97], [JRP02], tapes [TFG99], drums [MB02], flat polished disks [TF99]. To achieve the necessary precision, some of these setups use active stabilization circuits [MG98]. These examples are all based on solid-matter targets. They all have a problems with *debris* emission. The term debris stands for all kinds of material expelled from the target by the laser shot. This can be vapor, liquid droplets, small crystals or clusters. Debris can be a serious problem for sensitive optics or simply reduce the laser transmission into a vacuum chamber (see section 4.2.5). The severity of this problem led to the development of microscopic (10-80 micron) liquid-jet or droplet targets that can bring the mass of the target down to that of the number of required radiating atoms [JGR93]. These targets provide long term, low-debris or debris-free operation, with almost 4π illumination. However, so far they have been limited to only few liquids (water [RTD98], [VOG01], fluorocarbons [BRH98], copper nitrate solution [TMF98], ethylene glycol [TMF98]) and gases (N_2 [BRH98], [WWF01], Ar [WWF01], Xe [HRB00]). This is a drawback for hard x-ray generation at high laser intensities where high-Z materials have higher conversion efficiency. For the sake of completeness gas puff targets should be mentioned as well [FBP93]. They suffer from low particle density or high gas pressure.

In this work a new target system is presented, combining the advantages of microscopic liquid jet targets and those of metal targets by using a liquid metal jet as target system. Table 3-2 gives an overview of potential materials for a liquid metal target (water is added for comparison). Within this list gallium is by far the best candidate. It offers not only a very low melting point and a line radiation close to common Cu targets (K_α line for Cu is at 8 keV) but also convenient chemical (almost inert) and vacuum (vapor pressure at 771°C is 10^{-5} Torr [WE66]) properties. Mercury has a higher vapor pressure (0.1 Torr at 100°C [WE66]) and causes several handling problems because of its poisonous character. The advantage of a higher Z compared to gallium leads to higher efficiency in the generation of broadband bremsstrahlung. But, as it will be discussed in section 4.3.3, the difference is not remarkable.

Table 3-2 : Characteristics of liquid metals as candidates for laser-plasma target (Tm: melting point; T: temperature for the definition of the other constants; ρ: liquid density; σ: surface tension; η : viscosity; Z: atomic number; K_α: energy of line radiation) [CRC78].

	Tm (deg C)	T (deg C)	ρ (kg/m³)	σ (mN/m)	η (mPa s)	Z	K_α (keV)
Ga	29.8	37	6095	704	1.6	31	9.25
Se	221	250	4818	105	1.2	34	11.22
Rb	39	67	1463	91	0.5	37	13.39
In	156	250	7310	559	1.35	49	24.21
Cs	28	29	1850	73	1.2	55	30.97
Hg	-38.9	25	13594	484	1.52	80	70.82
Water	0	25	997	72	0.89	1.8	0.52

3.2.1 Fluid Dynamics of Microscopic Liquid Jets

The X-ray generation experiment defines two demands for the fluid dynamics of the jet target: It must have a certain velocity (to present each laser pulse a pristine surface) and the laminar part of the jet after the nozzle exit (before it is decaying into a stream of droplets) must be long enough to allow laser-focusing onto it. The jet velocity as well as the maximum length of the continuous jet filament can be calculated with a few hydrodynamic formulas [MF00]. In general, the jet behavior is determined by the nozzle diameter, *d*, the working pressure, *p*, and the material constants given in Table 3-2 (liquid density ρ; surface tension σ; viscosity η). To a good approximation, the flow velocity *v* of liquid jets entering a vacuum through a nozzle aperture is determined by the pressure *p* on the liquid reservoir and by the fluid density ρ:

$$v = \sqrt{\frac{2p}{\rho}} \quad . \qquad / \textbf{3-1}$$

Fig. 3-9 illustrates the development of the jet velocity at moderate pressures for three different materials. The velocity of 10 and 20 µm water jets was measured (using the jet-gap[1] propagation velocity) to be about 10% smaller than the calculated value, which is uncritical under the given experimental conditions. The minimum jet velocity is limited by two conditions: First, after laser illumination the jet is partially destroyed and forms an expanding gap. The jet velocity should be larger than this gap-expansion velocity which is about 8 m/s for gallium (nozzle diameter d = 30 µm) or for water with d = 20 µm, respectively. A second limitation is due to the laser repetition rate. But for rates of up to 10 kHz, as used in the experiments presented here, this condition is much weaker than the first. Measurements of Vogt [VOG02] determined maximum repetition rate for a 10 µm water-jet target to be greater than 250 kHz.
Another major concern for the work with liquid-jet targets is the length of the laminar part of the jet (jet decay length). The decay of the laminar jet is caused by surface waves which are amplified by capillary forces until the jet decays into a stream of droplets. For laminar flow conditions the decay length L depends on the jet velocity v, the liquid density ρ, the surface tension σ and the jet diameter d^* and can be estimated by [MF00]

$$L \approx 3.0\, v \sqrt{\frac{\rho\,(d^*)^3}{\sigma}}\ . \qquad / \textbf{3-2}$$

The jet diameter d^* is smaller than the nozzle diameter d because of a natural contraction of the jet after leaving the nozzle. Typical contraction factors range from d/d^*=0.6 to 0.9[MF00]. For nozzles comparable to the type used here, contraction factors of 0.63 for a nozzle orifice with a geometrical diameter of 10 µm, and of 0.80 to 0.85 for 20 µm and 50 µm, respectively

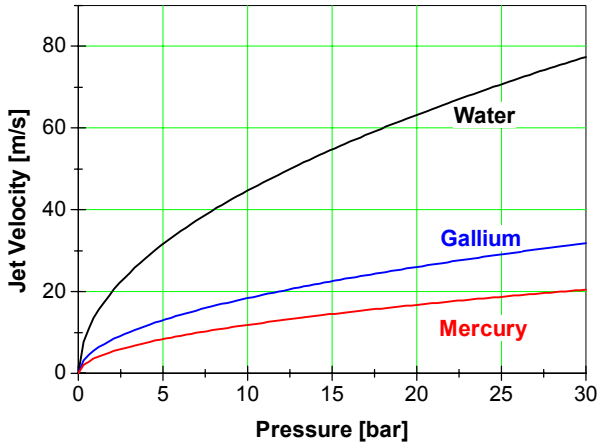

Fig. 3-9 : Jet velocity calculated for water, gallium and mercury.

[1] Details on the jet gap formation will be given in the next subsection.

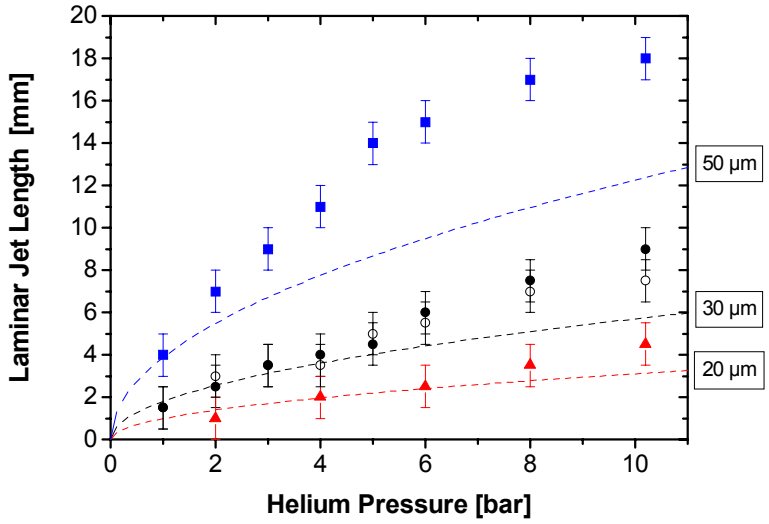

Fig. 3-10 : Laminar jet length of a water jet measured for different nozzle diameters (squares - 50µm, circles – 30 µm, triangles – 20 µm) compared with calculated values (dashed lines) for the respective diameter.

were found by laser diffraction measurements of the free liquid-jet diameter [MF00]. In Fig. 3-10 some measured decay lengths for water jest are compared to the numbers calculated using /3-2/. The contraction factors assumed for the calculation were 0.85 for d = 50 µm, 0.82 for d = 30 µm and 0.8 for d = 20 µm, respectively. Experimentally, the decay length was determined using the different diffraction of a He:Ne laser in the laminar and in the turbulent part of the jet. Apparently, the calculated values can be taken as a lower limit for the experimental numbers.

As one might expect, the laminar jet length can not be increased infinitely with ever larger pressure. At higher pressures the onset of turbulences limits the increase of the laminar jet length. This limit depends on the jet material constants and the jet diameter, d, and can be expressed using a reduced dimensionless variable (comparable to Reynolds number), the Ohnsorge number [MF00]:

$$Oh = \eta\left(\rho\sigma d\right)^{-1/2}. \qquad / 3\text{-}3$$

Using the Ohnsorge number, an empirical law for the maximum jet length before the onset of turbulence was found as [MF00]:

$$L_{\max} \leq 150\left(Oh\right)^{0.17}. \qquad / 3\text{-}4$$

Since the onset of turbulence strongly depends on the form and the quality of the nozzle orifices[1] used, the factor in /3-4/ might change depending on the nozzle. For fresh nozzles of the type used in this work, the factor was found to be about 600 [MF02]. This gives a maximum laminar length L_{max} of about 7 mm for a gallium jet (d = 30µm) and of 3.4 mm for a water jet (d = 10 µm). Based on equation /3-2/ and /3-4/, an optimum working pressure for particular experimental conditions (nozzle diameter, target material) can be calculated. The pressure should be low, to reduce target material consumption, but high enough to maintain the jet velocity v>10 m/s and the decay length $L \geq 2$ mm.

3.2.2 Jet apparatus

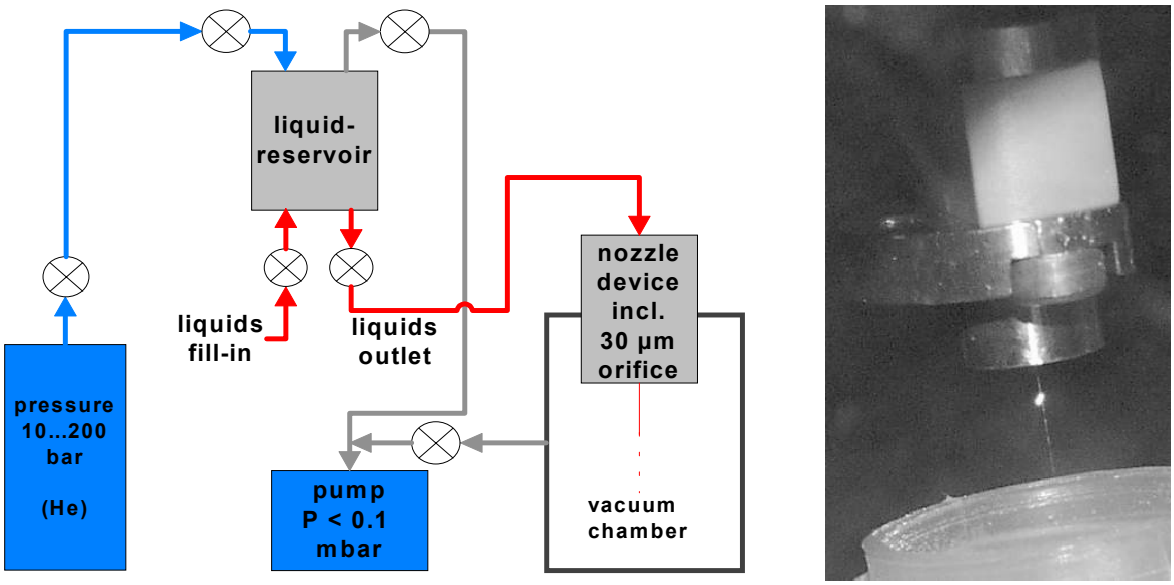

Fig. 3-11 : a) Schematic of the liqid-jet apparatus and b) photograph of the nozzle with a gallium jet and a plasma spark.

The jet apparatus is designed for non-interrupted operation during several hours, depending on the volume of the liquid reservoir. The gallium reservoir has a volume of 100 ml and allows for typical operation times of about 90 min (d = 30 µm, p = 20 bar). The water reservoir is larger (600 ml) and supports several hours of operation. Helium was chosen to provide the backing pressure at the reservoir because of its inert chemical character. Not shown in Fig. 3-11 is a particle filter (for particle size >2µm) in the nozzle apparatus to prevent blocking of the nozzle. The nozzle orifice is a diaphragm from electron microscopy (Plano GmbH, Wetzlar). The lifetime of such an orifice is a few hours for gallium experiments and some ten hours for water experiments.

[1] Mo and Pt nozzles for electron microscopy from Plano GmbH, Wetzlar..

3.2.3 Jet-gap measurements

The fluid dynamics theory outlined in section 3.2.1 describes the jet dynamics without laser interaction. But it does not give information on the jet behavior during and after the laser pulse. To investigate this question with appropriate temporal and spatial resolution, a setup for jet photography was built (Fig. 3-12). In this apparatus a green laser pulse (523 nm, 200 ns) was triggered by the main laser system and sent through the jet with tunable temporal delay. The shadow of the jet was projected with a lens (f = 50 mm) onto a screen outside the vacuum chamber. There, images of the magnified shadow were recorded with an Olympus C2500 digital camera. In this experiment the temporal behavior of a 20 µm water jet after exposure to strong laser pulses (2 mJ, 50 fs, 3×10^{16} W/cm²) was studied:

- Jet-gap formation

Within $t \leq 200$ ns after irradiation with the main laser pulse, a gap forms in the jet. During the first 600 ns ejection of target material perpendicular to the jet can be observed (Fig. 3-13). This material ejection strongly depends on the alignment: A small change (few µm) in the position of the laser focus on the jet leads to an asymmetric ejection. This is a qualitative prove for the high alignment precision (< 5 µm) and the jet stability (as well as the laser pointing stability).

- Jet-gap propagation

The gap moves with the jet and expands (Fig. 3-14). The gap expansion was measured in a sequence of photographs. The size of the nozzle (8 mm) served as scale in the images. In Fig. 3-15 the gap expansion is plotted for a 20 µm water jet with a backing pressure of 45 bar. The expansion is very rapid during the first microsecond, then the expansion velocity becomes

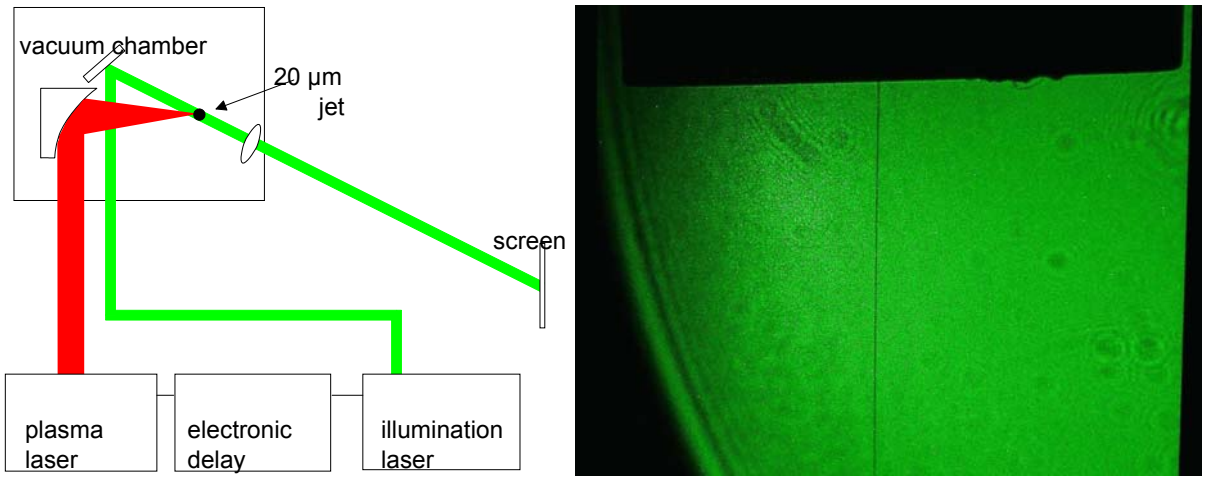

Fig. 3-12 : Schematic for the time-resolved jet photography and a typical picture of nozzle (top) and jet (the thin line from the nozzle downward, d = 20 µm) obtained with the apparatus.

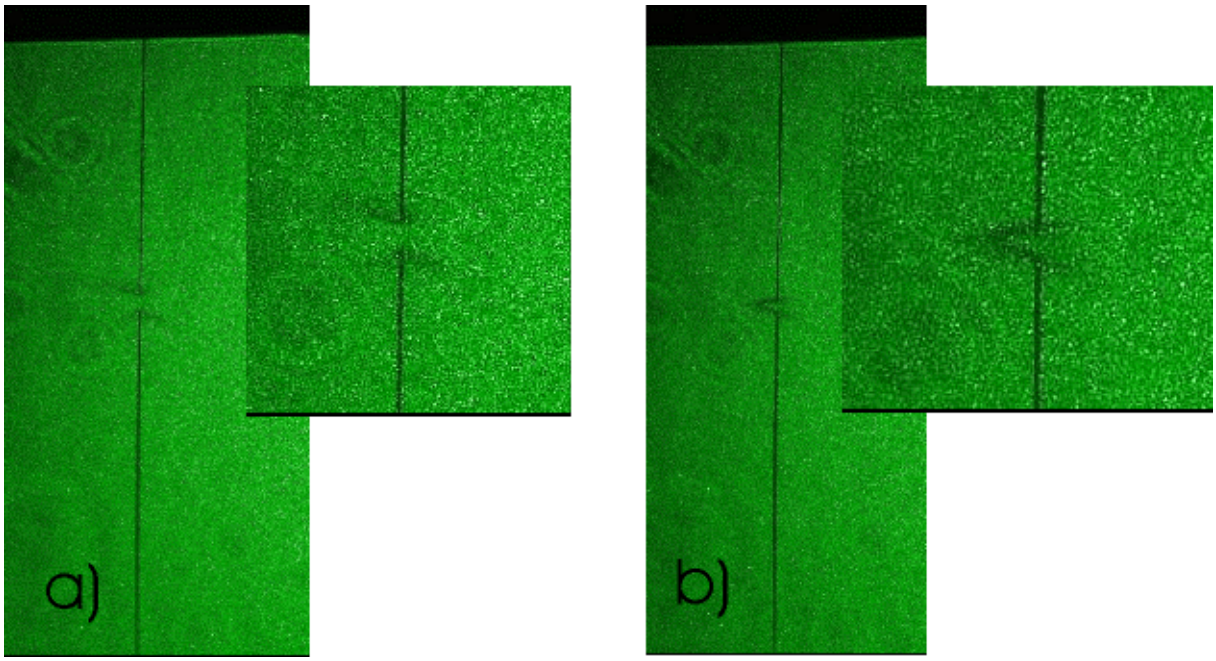

Fig. 3-13 : Jet photography after about 500 ns, a) with good alignment (symmetric evaporation from the jet-gap, see magnified inset), and b) small misalignment (asymmetric evaporation from the gap, see magnified inset).

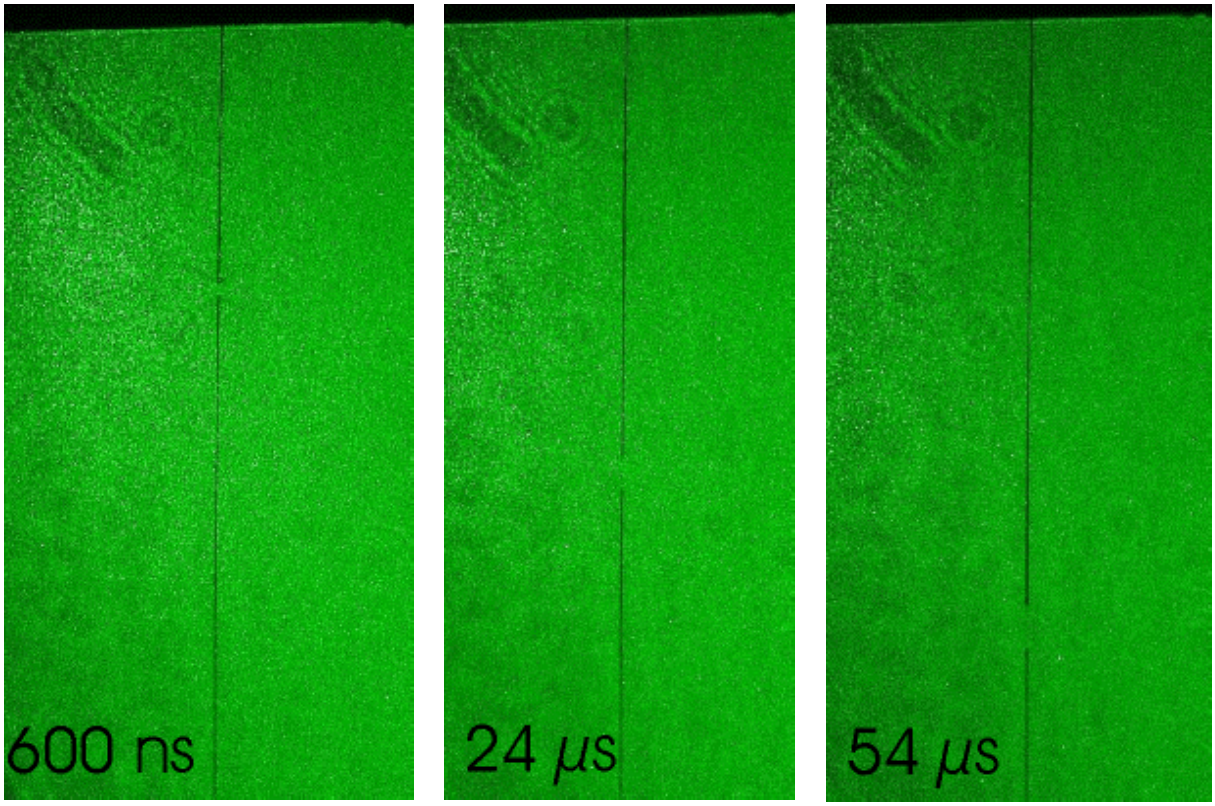

Fig. 3-14 : Photography of the jet with the jet-gap (moving top-down) with different time delays to the laser pulse.

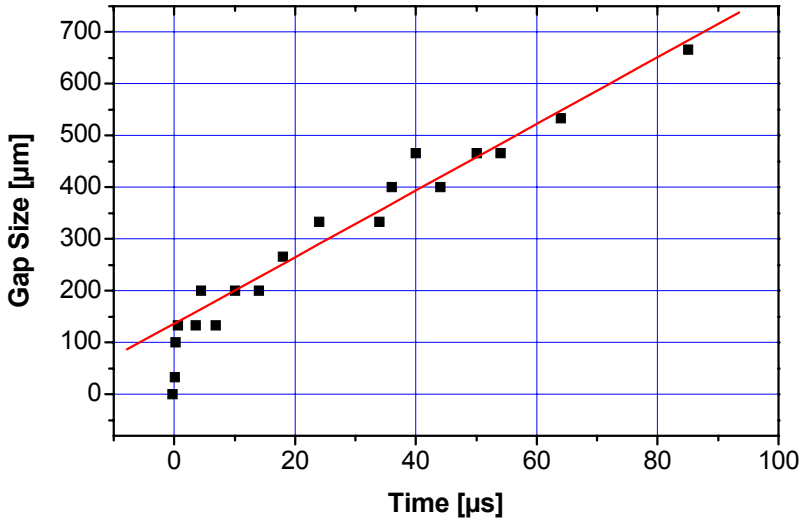

Fig. 3-15 : Expansion of the jet-gap, taken from stroboscopic photography. The line denotes a linear fit for the expansion velocity (v = 6.4 m/s).

linear. This linear expansion can be well explained by surface-tension forces. When the length of the open jet end is reduced by Δx, then its surface energy is reduced by $\Delta E = \Delta A \sigma$ (where $\Delta A = \Delta x * \pi d$). The corresponding force is $F = \sigma \pi d$. This force moves a mass dm with a velocity, u, into the jet, such that

$$\frac{dm}{dt} = \frac{\pi d^2}{4} u \rho \,. \qquad / \,3\text{-}5$$

Taking the change of the momentum of the mass element, dm:

$$\frac{dp}{dt} = u \frac{dm}{dt} = u^2 \frac{\pi d^2}{4} \rho \,, \qquad / \,3\text{-}6$$

and equating this with the surface-tension force, one obtains a formula for the contraction velocity of one end of the jet:

$$u = \sqrt{\frac{4\sigma}{\rho d}} \,. \qquad / \,3\text{-}7$$

For water the formula gives 3.8 m/s, which has to be doubled (two ends are contracting) and is than in a good agreement with the result of 6.4 m/s from a linear fit in the gap expansion curve Fig. 3-15.

Furthermore, one can deduce from the gap expansion an estimation for the amount of debris evaporated by the laser. With a gap size of about 100µm before contraction, one obtains 3×10^4 µm³ per laser shot or 1.9 mm³ per minute. This is a conservative approach, because it

assumes no contraction in the first 200 ns. For comparison: At a velocity of 20 m/s the jet flow is 377 mm^3/min.

In summary, from the jet photography several conclusions can be drawn: Firstly, the jet and the laser are spatially very stable (no instability of the jet was observed during the full experiment of more than 1 hour). Secondly, the laser produces in the jet a gap which limits the maximum repetition rate to, roughly estimated, 200 kHz (i.e. to 5 µs between consecutive pulses). This coincides with XUV-generation experiments at 250 kHz on a 10 µm water-jet target (signal breakdown was observed at 500 kHz [VOG02]). Thirdly, because no further jet decay happens after several hundred nanoseconds, the size of debris volume is roughly the product of the laser focal area multiplied by the jet diameter.